Micromechanics-based multiscale progressive failure simulation of 3D woven composites under compressive loading with minimal material parameters

Zheng, Tao; Guo, Licheng; Benedictus, Rinze; Pascoe, John Alan

DOI
10.1016/j.compscitech.2021.109227

Publication date
2022

Document Version
Final published version

Published in
Composites Science and Technology

Citation (APA)
Zheng, T., Guo, L., Benedictus, R., & Pascoe, J. A. (2022). Micromechanics-based multiscale progressive failure simulation of 3D woven composites under compressive loading with minimal material parameters. *Composites Science and Technology*, *219*, Article 109227. https://doi.org/10.1016/j.compscitech.2021.109227

Composites Science and Technology 219 (2022) 109227

Contents lists available at ScienceDirect

Composites Science and Technology

journal homepage: www.elsevier.com/locate/compscitech

Micromechanics-based multiscale progressive failure simulation of 3D woven composites under compressive loading with minimal material parameters

Tao Zheng [a,b], Licheng Guo [a,*], Rinze Benedictus [b], John-Alan Pascoe [b,**]

[a] Department of Astronautic Science and Mechanics, Harbin Institute of Technology, Harbin, 150001, PR China
[b] Structural Integrity and Composite Group, Faculty of Aerospace Engineering, Delft University of Technology, the Netherlands

ARTICLE INFO

Keywords:
A. Polymer-matrix composites (PMCs)
A. Textile composites
B. Non-linear behaviour
C. Multiscale modeling
C. Representative volume element (RVE)

ABSTRACT

A novel micromechanics-based multiscale progressive damage model, employing minimal material parameters, is proposed in this paper to simulate the compressive failure behaviours of 3D woven composites (3DWC). The highly realistic constructions of microscopic and mesoscopic representative volume cells are accomplished, and a set of strain amplification factor is employed to bridge the meso-scale and micro-scale numerical calculations. Considering that the multiple failure mechanisms of 3DWC under compression are all caused by the matrix failure from the microscopic perspective, a new method incorporating the micromechanics of failure (MMF) theory and 3D kinking model is developed to identify the micro matrix failure associated with the kinking of yarns, inter-fiber fracture and pure matrix failure. As a result, only the matrix parameters are required for the failure simulation of 3DWC, eliminating the necessity of using other material parameters such as the fracture toughness and failure strengths of fiber yarns, which are generally difficult to accurately obtain through experiments. The newly proposed damage model is numerically integrated into ABAQUS with a user-defined subroutine UMAT. The numerical predictions and the experimental results exhibit good agreement, verifying the feasibility and accuracy of the novel damage model.

1. Introduction

Benefiting from the three-dimensional spatial reinforcement architecture, 3D woven composites (3DWC) are extensively used in aerospace, aeronautics and national defense fields owing to the attractive superiorities of near-net-shape adaptability, better impact resistance and high structural integrity with respect to traditional laminates [1,2]. In actual applications, composite structures are inevitably subjected to compressive loading conditions. However, the compressive properties of composites are much inferior to the tensile properties [3], which greatly limits the wide usages of composite materials. Moreover, the failure mechanisms of 3DWC under compression are very complicated because of the complex reinforcement architecture. Many experimental investigations have been conducted by Waas group at the University of Michigan to reveal the compressive failure mechanisms of textile composites [4–8]. Quek and Waas [4] first experimentally investigated the biaxial compression/tension performance of braided composites. The experimental results indicated that the buckling and kinking of yarns are the dominant failure mechanisms. Then Pankow et al. [5] studied the high strain rate dependent compressive responses of 3DWC through split Hopkinson pressure bar (SHPB) testing. The effects of Z-pins on the compressive strength of Z-pinned woven composites have been evaluated by Huang and Waas [6]. It was found that the initial damage zone caused by Z-pins insertion reduces the compressive strength. Subsequently, the flexural and compressive progressive failure responses of hybrid 3D textile composites were experimentally studied by Zhang et al. [7] and Patel et al. [8], respectively. Recently, Zheng et al. [9] conducted an experimental investigation on the compression properties of 3DWC. It was observed that the kinking of longitudinal yarns, inter-fiber fracture, pure matrix failure and interface debonding are the primary competing mechanisms within 3DWC. Although the main failure mechanisms can be obtained through the final fracture morphologies of macroscopic specimens, the initiations and evolutions of each failure mechanism cannot be isolated for independent analysis.

* Corresponding author.
** Corresponding author.
E-mail addresses: guolc@hit.edu.cn (L. Guo), j.a.pascoe@tudelft.nl (J.-A. Pascoe).

https://doi.org/10.1016/j.compscitech.2021.109227
Received 23 September 2021; Received in revised form 16 December 2021; Accepted 19 December 2021
Available online 21 December 2021

Consequently, high-accuracy numerical models are essential to fully understand the compressive loading behaviors and damage progressions of 3DWC.

Progressive damage models have proven to be a promising approach to investigating the failure mechanisms of textile composites, where the damage initiations are determined by criteria and the stiffness degradations are governed by damage evolution models. Many phenomenological failure criteria were put forward to identify the damage initiations of composite materials. Hashin [10] firstly proposed four quadratic formulas to identify the tension and compression fiber and matrix damage modes of unidirectional composites. After that Chang [11] introduced the material nonlinearity to the Hashin criterion, based on which Lessard [12] proposed the concept of in-situ strength and derived a fiber buckling failure criterion. In an attempt to improve the predictions of inter-fiber failure, Hashin criterion has been modified by Puck [13,14] by taking the action plane concept and Mohr-Coulomb friction into account. Derived from Puck's action plane proposal, the physically based LaRC criteria [15,16] were also well-established to predict the inter-fiber failure and fiber kinking. However, all the criteria mentioned above are developed at the meso-scale based on the assumption that composites are regarded as homogeneous materials. This assumption is still questionable because the composite materials are actually composed of fiber and resin constituents with distinct material properties. To independently determine the damage initiations of fiber filaments and resin at the microscopic scale, Ha et al. [17] proposed the micromechanics of failure (MMF) theory by employing the stress and strain amplification factor (SSAF) [18]. For different load conditions and material systems of composites, MMF theory has exhibited prominent prediction capabilities [19,20]. Based on fully analytical solutions, Zhang and Waas [21] and Patel et al. [22] proposed the 2-CYL and NCYL concentric cylinder models to calculate the spatial strain and stress distributions within the fiber and resin constituents, which provides a distinct computational efficiency for the multiscale analysis of composite structure.

In addition to predicting the onset of damage, appropriate damage evolution models need to be employed to control the evolutions of damage variables. The simplest form of damage evolution model is the stiffness reduction method [23,24]. Once the failure criteria are activated, the material properties directly degrade to a small magnitude, ignoring the gradual fracture process. However, according to Fang et al. [25], the empirical magnitudes of stiffness reduction present a significant impact on the damage behaviors of composites. Moreover, the stiffness reduction method will inevitably lead to strong mesh dependence of numerical predictions [26]. To alleviate the mesh dependence, a crack band theory was developed by Bažant [27], based on which multiple damage evolvement schemes depending on fracture toughness have been subsequently developed. Maimí [28] proposed an exponential evolvement model to capture the brittle fracture of composites, which effectively alleviates the mesh dependence problem. For easier numerical implementation, a bilinear damage evolution model controlled by equivalent displacement has been developed by Lapczyk [26]. Based on a smeared crack approach, Zhang et al. [29] designed different traction-separation laws to differentiate the tensile and compressive damage evolutions of fiber tows. Subsequently, Zhong [30] and He [31] employed the linear and exponential evolvement schemes to simulate the fiber pull-out and bridging phenomena. It should be noted that the fracture toughness associated with different damage modes of fiber yarns are difficult to accurately measure through experiments. For the damage evolution prediction of fiber yarns, most scholars quoted the fracture toughness of similar material systems from other literature [28, 31–34]. In some cases, scholars artificially assumed the values of fracture toughness [25,26,35], which would bring uncertainty and weaken the reliability of simulation results. Furthermore, the fiber yarns inside 3D textile composites with different fiber volume fractions will undoubtedly possess different fracture toughness, which further increases the difficulty of the experimental measurements. Therefore, how to use minimal material parameters to simulate the failure behaviors of 3DWC with high accuracy is an urgent problem to be solved.

This paper proposes a novel micromechanics-based multiscale damage model to investigate the compressive failure behaviours of 3DWC with minimal material parameters. With the built-in functions and Python scripts of TexGen, the highly realistic constructions of microscopic and mesoscopic representative volume cells (RVC) are first accomplished. Then the MMF theory is applied to bridge the meso-scale and micro-scale calculations by employing a set of SSAF. From the microscopic perspective, the compressive failure mechanisms of 3DWC, including the kinking of yarns, inter-fiber fracture and pure matrix failure, are caused by the damage of matrix. Consequently, a new method incorporating the MMF theory and three-dimensional kinking model is developed to identify the micro matrix failure within the fiber yarns. As a result, only matrix parameters are required to predict the damage initiations and evolutions, eliminating the necessity of using other material parameters that are generally difficult to accurately obtain through experiments. The compressive effective properties and damage accumulations of 3DWC are predicted by the newly proposed multiscale damage model and compared with the corresponding experiments.

2. Multiscale modeling based on MMF theory

2.1. Mesoscopic representative volume cell (RVC)

As presented in Fig. 1(a), 3D woven composites are composed of fiber tows, matrix and tow/matrix interfaces at meso-scale, and the tows can be further divided into three categories: binder, weft and warp tows. The warp and weft layers are vertically distributed in the plane, along the global X and Y direction, respectively. To enhance the out-of-plane performance and integrity of the composites, the binder bundles are designed to interlock with weft tows in the thickness direction. The matrix phase for all impregnated bundles is TDE-86 epoxy resin. The reinforced phase of warp and weft tows is T700-12K carbon fibers, and the reinforced phase of binder tows is T300-3K fibers. The material properties of reinforced T700 and T300 fibers and TDE-86 matrix are listed in Table 1.

Because the geometric structure of 3DWC is periodic, a mesoscopic RVC illustrated in Fig. 1(b) is identified to simulate the overall woven architecture. The material geometry of the top and bottom-most layers is different to that of the bulk composite. However, these layers represent only a small portion of the total material volume, and there is no reason to assume failure would initiate specifically in those layers. Therefore, to reduce the computational cost of the model, it is chosen to only create an RVC based on the internal geometry of the composites. It is noted the geometry modeling of the RVC is carried out in the TexGen software. With the built-in functions and Python scripts of TexGen, the cross sections and undulating paths of yarns can be generated parametrically, allowing for more realistic reconstruction of the woven architecture. The warp and weft tows are created by sweeping several ellipse cross-sections along an undulating path defined by sinusoidal functions, and the cross-sections of binder are constructed by lenticular functions. The detailed geometric parameters of the RVC can be seen in Ref. [36]. Given that the geometric structure of the meso RVC is complex, the C3D4 elements with good boundary adaptability are adopted for mesh discretization. Because of the requirement of imposing periodic boundary conditions, the meshes on opposite boundaries need to be consistent. In addition, a Python script was compiled to automatically apply boundary constraints to the corresponding node pairs. To characterize the interface debonding between yarns and matrix, zero-thickness cohesive elements (COH3D6) shown in Fig. 1(e) are created according to the common coordinates of tow and matrix elements.

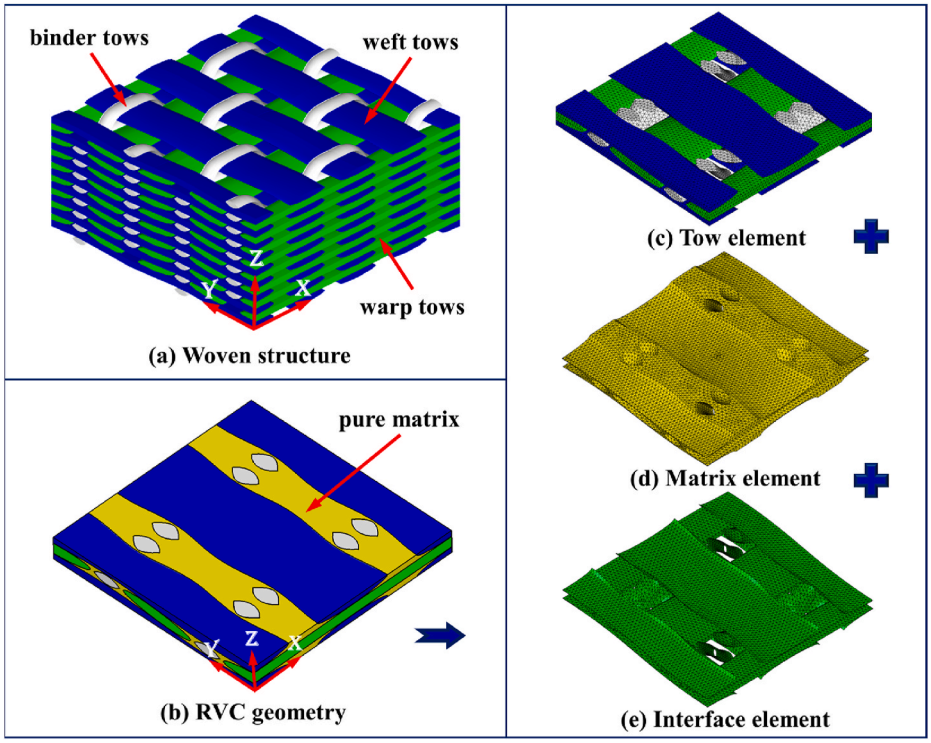

Fig. 1. Geometric structure and mesoscopic RVC of 3D woven composites.

Table 1
The material properties of reinforced carbon fibers and TDE-86 matrix [30].

Fiber: T700	Fiber: T300	Matrix: TDE-86
E_{f11} (GPa) = 230.0	E_{f11} (GPa) = 221.0	E_m (GPa) = 3.55
E_{f22} (GPa) = 18.20	E_{f22} (GPa) = 13.81	ν_m = 0.33
G_{f12} (GPa) = 36.62	G_{f12} (GPa) = 9.00	m_t (MPa) = 80.0
ν_{f12} = 0.27	ν_{f12} = 0.20	m_c (MPa) = 241.0
ν_{f23} = 0.30	ν_{f23} = 0.25	$G_{C,m}$ (N/mm) = 1.0 [25]

2.2. Microscopic representative volume cell

At the microscale level, the fiber yarns within 3DWC are generally regarded as a unidirectional lamina. The effective performances of this unidirectional lamina can be characterized by the microscopic RVC with hexagonal fiber distributions over the cross section perpendicular to the fibers. Jin and Huang [18,37] have confirmed that for high fibre volume fractions ($V_f \geq 75\%$) a random packing trends towards a hexagonal configuration. As the V_f of the tows in the present case exceeds 75%, a hexagonal distribution is considered suitable to simulate the properties of yarn bundles. As illustrated in Fig. 2, L and W respectively represent the length and width of the micro RVC, which are both equal to 1, and H is the height and equal to $\sqrt{3}$. Once the fiber volume fraction of yarns is determined, the fiber radius can be calculated by $R = \sqrt{\sqrt{3}V_f/(2\pi)}$. Through the micro RVC, not only the elastic constants of the yarns can be according to the properties of the constituents, but also the strain and stress distribution of pure fibers and micro matrix can be determined, which makes it feasible to judge the microscopic failure based on the MMF theory [17].

2.3. Strain and stress amplification factor (SSAF)

In this paper, the micromechanics of failure (MMF) [17] is employed to bridge the mesoscopic and microscopic calculations. By employing the strain and stress amplification factor, the strain and stress components of constituents at the micro scale can be calculated by the stress

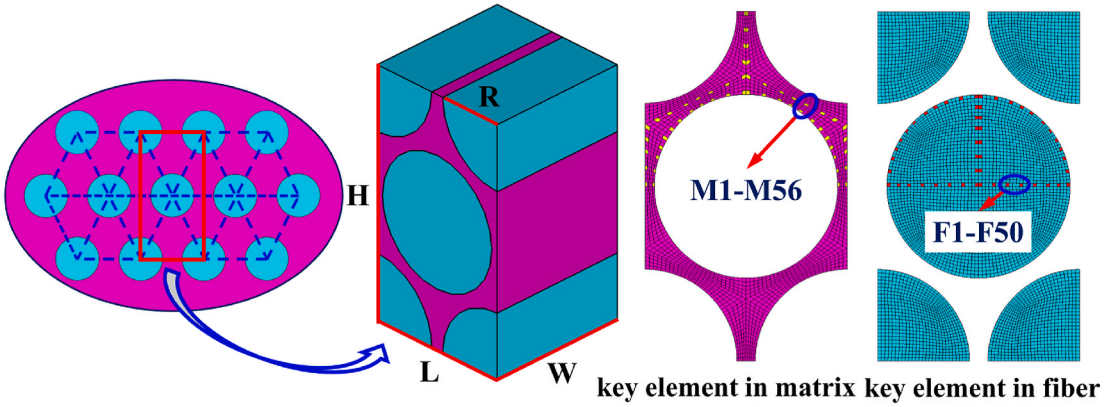

Fig. 2. Microscale representative volume cell and key elements in fibers and matrix.

and strain components of fiber yarns at the meso scale. The SSAF can be defined as follows:

$$\begin{cases} \boldsymbol{\sigma}_{ff} = \mathbf{M}_{f,\sigma}\overline{\boldsymbol{\sigma}}_f;\ \boldsymbol{\sigma}_{fm} = \mathbf{M}_{m,\sigma}\overline{\boldsymbol{\sigma}}_f \\ \boldsymbol{\varepsilon}_{ff} = \mathbf{M}_{f,\varepsilon}\overline{\boldsymbol{\varepsilon}}_f;\ \boldsymbol{\varepsilon}_{fm} = \mathbf{M}_{m,\varepsilon}\overline{\boldsymbol{\varepsilon}}_f \end{cases} \tag{1}$$

where $\mathbf{M}_{f,\sigma}$ and $\mathbf{M}_{m,\sigma}$ indicate the stress amplification factor of the fiber and matrix within micro RVC, respectively, and $\mathbf{M}_{f,\varepsilon}$ and $\mathbf{M}_{m,\varepsilon}$ indicate the strain amplification factors. It is noted that $\overline{\boldsymbol{\sigma}}_f$, $\boldsymbol{\sigma}_{ff}$, and $\boldsymbol{\sigma}_{fm}$ denote the meso stress of tows, micro stress of pure fiber and matrix, respectively, and $\overline{\boldsymbol{\varepsilon}}_f$, $\boldsymbol{\varepsilon}_{ff}$, and $\boldsymbol{\varepsilon}_{fm}$ denote the corresponding strain components. The complete forms of Eq (1) can be expressed as follows [18]:

$$\begin{cases} \begin{pmatrix} \sigma_{11} \\ \sigma_{22} \\ \sigma_{33} \\ \tau_{12} \\ \tau_{13} \\ \tau_{23} \end{pmatrix}_{\substack{ff \\ fm}} = \begin{bmatrix} M_{\sigma11} & M_{\sigma12} & M_{\sigma13} & 0 & 0 & M_{\sigma16} \\ M_{\sigma21} & M_{\sigma22} & M_{\sigma23} & 0 & 0 & M_{\sigma26} \\ M_{\sigma31} & M_{\sigma32} & M_{\sigma33} & 0 & 0 & M_{\sigma36} \\ 0 & 0 & 0 & M_{\sigma44} & M_{\sigma45} & 0 \\ 0 & 0 & 0 & M_{\sigma54} & M_{\sigma55} & 0 \\ M_{\sigma61} & M_{\sigma62} & M_{\sigma63} & 0 & 0 & M_{\sigma66} \end{bmatrix} \begin{pmatrix} \overline{\sigma}_{f11} \\ \overline{\sigma}_{f22} \\ \overline{\sigma}_{f33} \\ \overline{\tau}_{f12} \\ \overline{\tau}_{f13} \\ \overline{\tau}_{f23} \end{pmatrix} \\ \begin{pmatrix} \varepsilon_{11} \\ \varepsilon_{22} \\ \varepsilon_{33} \\ \gamma_{12} \\ \gamma_{13} \\ \gamma_{23} \end{pmatrix}_{\substack{ff \\ fm}} = \begin{bmatrix} 1 & 0 & 0 & 0 & 0 & 0 \\ M_{\varepsilon21} & M_{\varepsilon22} & M_{\varepsilon23} & 0 & 0 & M_{\varepsilon26} \\ M_{\varepsilon31} & M_{\varepsilon32} & M_{\varepsilon33} & 0 & 0 & M_{\varepsilon36} \\ 0 & 0 & 0 & M_{\varepsilon44} & M_{\varepsilon45} & 0 \\ 0 & 0 & 0 & M_{\varepsilon54} & M_{\varepsilon55} & 0 \\ M_{\varepsilon61} & M_{\varepsilon62} & M_{\varepsilon63} & 0 & 0 & M_{\varepsilon66} \end{bmatrix} \begin{pmatrix} \overline{\varepsilon}_{f11} \\ \overline{\varepsilon}_{f22} \\ \overline{\varepsilon}_{f33} \\ \overline{\gamma}_{f12} \\ \overline{\gamma}_{f13} \\ \overline{\gamma}_{f23} \end{pmatrix} \end{cases} \tag{2}$$

Because the stress and strain can be converted through constitutive equations at each scales, the relations between the strain and stress amplification factors can be derived as follows:

$$\begin{cases} \boldsymbol{\sigma}_{fm} = \mathbf{M}_{m,\sigma}\overline{\boldsymbol{\sigma}}_f \Rightarrow \mathbf{C}_m\boldsymbol{\varepsilon}_{fm} = \mathbf{M}_{m,\sigma}\overline{\mathbf{C}}_f\overline{\boldsymbol{\varepsilon}}_f \Rightarrow \boldsymbol{\varepsilon}_{fm} = \mathbf{C}_m^{-1}\mathbf{M}_{m,\sigma}\overline{\mathbf{C}}_f\overline{\boldsymbol{\varepsilon}}_f \\ \text{and } \boldsymbol{\varepsilon}_{fm} = \mathbf{M}_{m,\varepsilon}\overline{\boldsymbol{\varepsilon}}_f \Rightarrow \text{ so } \mathbf{M}_{m,\varepsilon} = \mathbf{C}_m^{-1}\mathbf{M}_{m,\sigma}\overline{\mathbf{C}}_f \end{cases} \tag{3}$$

where $\mathbf{C}_m$ and $\overline{\mathbf{C}}_f$ are the stiffness constitutive equations of the matrix and fiber yarns respectively. Therefore, in the actual calculation, it is enough to obtain the stress amplification factor, then the corresponding strain amplification factor can be calculated by Eq (3). Alternatively, the strain amplification factor can be obtained first, and then converted to obtain the stress amplification factor. As for the calculation of SSAF, a set of microanalyses on the micro RVC needs to be carried out. Due to the uneven distributions of stress and strain in the micro RVC, a total of 50 fiber key elements and 56 matrix key elements shown in Fig. 2 are chosen as representatives. A parameter study has been conducted to prove the numbers of key elements are sufficient to obtain the convergent SSAF. It was observed that the SSAFs obtained when using 2496 key materix elements were identical to those obtained using only 56 key elements. Therefore 56 key elements were considered sufficient. Six normalized meso stress cases are sequentially loaded on the micro RVC to calculate each column of the SAF matrix as follows. When the unit meso stress $\overline{\boldsymbol{\sigma}}_f = [1,\ 0,\ 0,\ 0,\ 0,\ 0]^T$ is applied, the stress components of each key element can be extracted, which allows the first column of $\mathbf{M}_{f,\sigma}$ and $\mathbf{M}_{m,\sigma}$ to be calculated. The remaining five columns can be obtained by the same method, applying a unit load for the corresponding stress component, and setting the other components to zero.

3. Compressive failure mechanisms of 3DWC

According to the experimental observations as illustrated in Fig. 3 [9], there are four primary failure mechanisms within 3DWC under compressive loadings, which are kinking of fiber yarns in longitudinal direction, inter-fiber fracture in transverse direction, pure matrix failure and yarns/matrix interface debonding. In this section, each failure mechanism is introduced separately and the corresponding damage initiation and evolution are also considered.

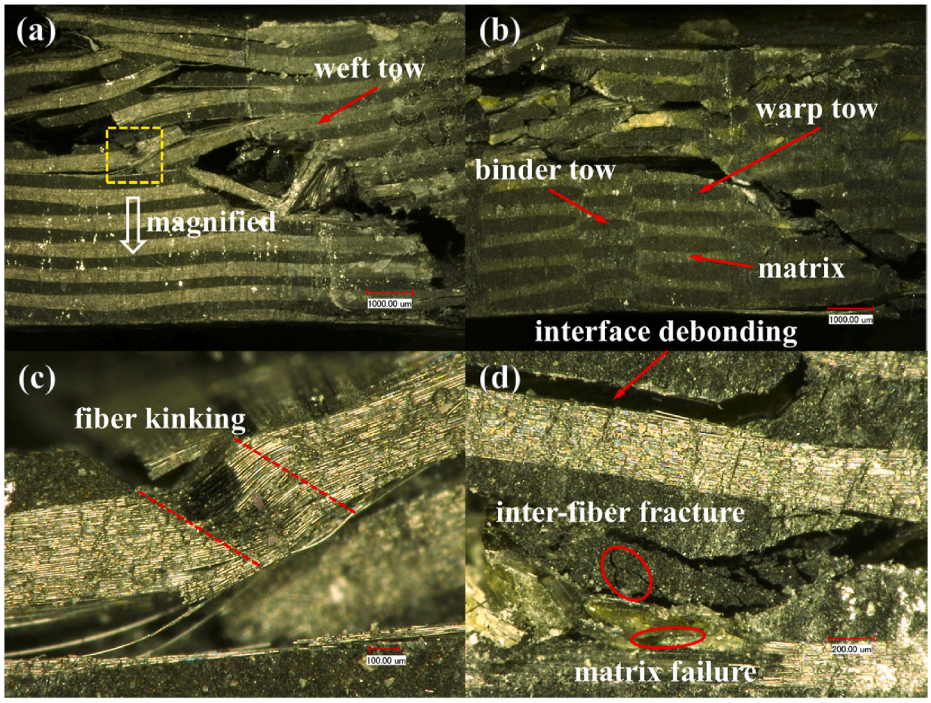

Fig. 3. Primary failure mechanisms within 3DWC under compressive loadings [9].

3.1. Pure matrix failure and progressive damage model

Although the matrix can be regarded as isotropic, it presents different tension and compression strengths. Both the von Mises stress σ_{VM} and first stress invariant I_1 contribute to the damage initiation of matrix. In order to consider these two stress components, Raghava [38] proposed a modified von Mises failure criterion.

$$\varphi_m = \frac{\sqrt{4m_t m_c \sigma_{VM}^2 + (m_c - m_t)^2 I_1^2} + (m_c - m_t) I_1}{2m_t m_c} \tag{4}$$

where m_t and m_c denote the matrix tension and compression strengths. The concept of equivalent stress is generally employed to transform complex multiaxial stress-strain relationships into uniaxial simple stress-strain relationships. Based on the failure criterion, the equivalent stress $\sigma_{eq,m}$ of matrix can be deduced as follows:

$$\sigma_{eq,m} = \left[\sqrt{4m_t m_c \sigma_{VM}^2 + (m_c - m_t)^2 I_1^2} + (m_c - m_t) I_1\right] \Big/ (2m_c) \tag{5}$$

$\sigma_{eq,m}$ defined by Eq. (5) can be also called Stassi's equivalent stress [39]. According to Huang et al. [20], the matrix failure occurs when $\sigma_{eq,m}$ exceeds the tensile strength m_t. Correspondingly, the equivalent displacement $\delta_{eq,m}$ of matrix under complex multiaxial stress condition can be calculated based on the stress-strain relation.

$$\delta_{eq,m} = l_{c,m} \frac{\sqrt{\left(\frac{2-4\nu_m}{1+\nu_m}\right)^2 m_t m_c \varepsilon_{VM}^2 + (m_c - m_t)^2 J_1^2} + (m_c - m_t) J_1}{2m_c(1-2\nu_m)} \tag{6}$$

Where $l_{c,m}$ is characteristic element length, and the detailed expressions of the first strain invariant J_1 and von Mises strain ε_{VM} can be written as follows:

$$\begin{cases} J_1 = \varepsilon_{m11} + \varepsilon_{m22} + \varepsilon_{m33} \\ \varepsilon_{VM} = \dfrac{1}{\sqrt{2}} \sqrt{\begin{array}{c} (\varepsilon_{m11} - \varepsilon_{m22})^2 + (\varepsilon_{m11} - \varepsilon_{m33})^2 + (\varepsilon_{m22} - \varepsilon_{m33})^2 + \\ 3\left(\gamma_{m12}^2 + \gamma_{m13}^2 + \gamma_{m23}^2\right)/2 \end{array}} \end{cases} \tag{7}$$

To alleviate the mesh dependency, a bilinear damage evolution model [25], controlled by fracture toughness $G_{C,m}$, as well as $\delta_{eq,m}$ and $l_{c,m}$, is adopted to control the damage evolution of matrix. The damage variable d_m, tracking the matrix failure, can be defined as follows:

$$d_m = 1 - \frac{\delta_{eq,m}^i \left(\delta_{eq,m}^u - \delta_{eq,m}\right)}{\delta_{eq,m} \left(\delta_{eq,m}^u - \delta_{eq,m}^i\right)}, \quad \delta_{eq,m}^i \le \delta_{eq,m} \le \delta_{eq,m}^u \tag{8}$$

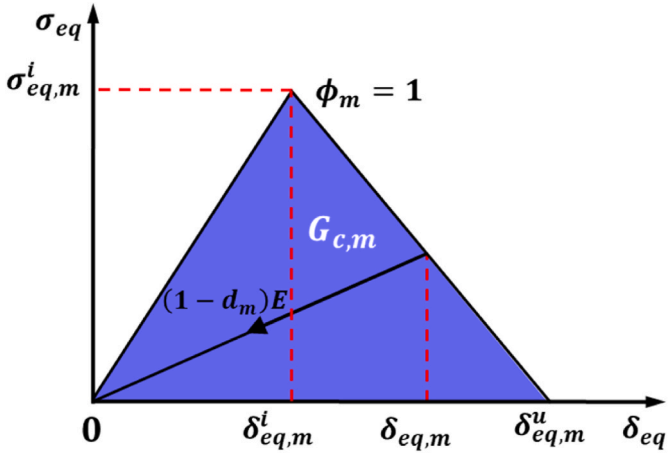

Fig. 4. The bilinear damage evolvement model for the pure matrix.

where $\delta_{eq,m}^i$ is the equivalent displacement corresponding to the initial matrix failure, and $\delta_{eq,m}^u$ corresponds to the ultimate damage state as indicated in Fig. 4. As mentioned above, the equivalent stress corresponding to the initial matrix failure is equal to m_t, that is $\sigma_{eq,m}^i = m_t$. Therefore, $\delta_{eq,m}^i$ and $\delta_{eq,m}^u$ can be simply calculated through the following relations:

$$\begin{cases} \delta_{eq,m}^i = l_{c,m}\sigma_{eq,m}^i \Big/ E_m = l_{c,m} m_t \Big/ E_m \\ \delta_{eq,m}^u = 2G_{C,m} \Big/ \sigma_{eq,m}^i = 2G_{C,m} \Big/ m_t \end{cases} \tag{9}$$

where $G_{C,m}$ denotes the fracture toughness. In Eq. (8), $\delta_{eq,m}^i$ and $\delta_{eq,m}^u$ can be calculated by material parameters. So as long as the equivalent displacement $\delta_{eq,m}$ is calculated by Eq. (6), the corresponding damage variable d_m can be directly obtained without using the stress components of the matrix, which greatly simplifies the actual numerical calculations.

3.2. Transverse inter-fiber fracture of yarns

Inter-fiber fracture of fiber yarns in transverse direction is a common damage mode within 3D woven composites, which is caused by matrix failure inside fiber bundles at the micro-scale. According to the MMF theory, the strain components of the yarns can be converted into the strain components of matrix in the micro RVC through the strain amplification factors. In actual calculations, the damage status on 56 matrix key elements needs to be checked in turn. When one of the elements satisfies the failure criterion, the inter-fiber fracture of yarns is considered to be initiated. As mentioned in Section 3.1, it is only necessary to calculate the equivalent displacement of matrix, then the damage variable can be directly obtained. In this paper, $d_{f,m}$ is defined as the damage variable associated with inter-fiber fracture of yarns.

$$d_{f,m} = 1 - \frac{\delta_{eq,m}^i \left(\delta_{eq,m}^u - \delta_{eq,fm}\right)}{\delta_{eq,fm} \left(\delta_{eq,m}^u - \delta_{eq,m}^i\right)}, \quad \delta_{eq,fm} = \max\left(\delta_{eq,fm}^{(K)}\right), \ K \in [1,\ 56] \tag{10}$$

3.3. Kinking of yarns in longitudinal direction

The kinking of yarns in longitudinal direction is initiated by initial fiber misalignments or microstructural defects [3]. According to Argon [40], the initial fiber misalignment results in certain shear stresses

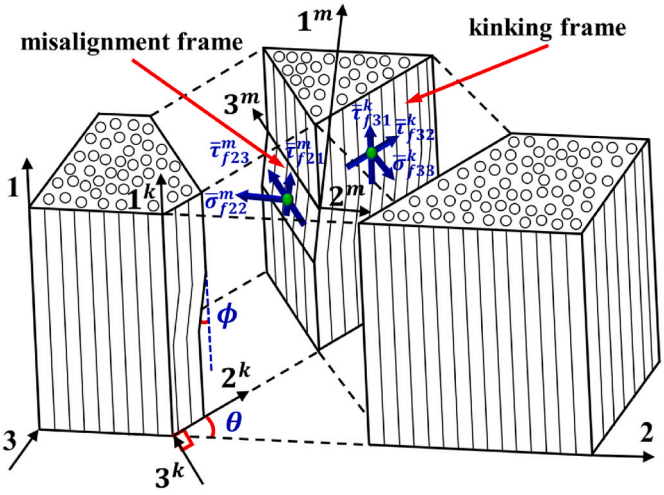

Fig. 5. 3D kinking model of fiber yarns under complex stress states.

within yarns under axial compression, then these shear stresses would produce shear strain to further increase the misalignment angle of fiber, which will in turn increase the shear stress. Finally, once the matrix stresses between fibers satisfy the failure criterion, the kinking failure of yarns occurs. In this paper, a novel method incorporating the MMF theory [17] and 3D kinking model [16] is developed to identify the kinking failure of yarns. The axial frame ($1-2-3$), misalignment frame ($1^m-2^m-3^m$) and kinking frame ($1^k-2^k-3^k$) of yarns under complex stress states are illustrated in Fig. 5. The relationships between different coordinate frames are as follows: $1-2-3$ rotates θ degrees around 1 axis to get $1^k-2^k-3^k$, and $1^k-2^k-3^k$ rotates φ degrees around 3^k axis to get $1^m-2^m-3^m$. It is noted that $\overline{\boldsymbol{\sigma}}_f$, $\overline{\boldsymbol{\sigma}}_f^k$, and $\overline{\boldsymbol{\sigma}}_f^m$ are the stresses of yarns corresponding to the axial frame, kinking frame and misalignment frame, respectively, and $\overline{\boldsymbol{\varepsilon}}_f$, $\overline{\boldsymbol{\varepsilon}}_f^k$, and $\overline{\boldsymbol{\varepsilon}}_f^m$ denote the related strains. The angles θ and φ are functions of the meso stresses of the fiber yarns and the initial misalignment angle φ_0.

$$\theta=\arctan\left(\frac{2\overline{\tau}_{f23}}{\overline{\sigma}_{f22}-\overline{\sigma}_{f33}}\right)\Big/2,\ \varphi=\frac{\varphi_0 G_{f12}+\left|\overline{\tau}_{f12}^k\right|}{G_{f12}+\overline{\sigma}_{f11}^k-\overline{\sigma}_{f22}^k} \tag{11}$$

In this paper, $d_{f,kink}$ is defined to correlate the kinking failure of yarns. It is known from Section 3.1 that the matrix failure within $1^m-2^m-3^m$ frame can be simply determined by calculating the equivalent displacement of the micro matrix through Eqs. (6) and (8). As a result, $d_{f,kink}$ can be obtained by the following equations:

$$d_{f,kink}=1-\frac{\delta_{eq,m}^i\left(\delta_{eq,m}^u-\delta_{eq,fm}^m\right)}{\delta_{eq,fm}^m\left(\delta_{eq,m}^u-\delta_{eq,m}^i\right)},\ \delta_{eq,fm}^m=\max\left(\delta_{eq,fm}^{m\ (K)}\right),\ K\in[1,\ 56] \tag{12}$$

where $\delta_{eq,fm}^{m\ (K)}$ denotes the equivalent displacement of K-th matrix key element, which is calculated from the micro strains $\boldsymbol{\varepsilon}_{fm}^{m\ (K)}$ of the matrix in misalignment frame. $\boldsymbol{\varepsilon}_{fm}^{m\ (K)}$ can be calculated by the strain amplification factor as follows:

$$\boldsymbol{\varepsilon}_{fm}^{m\ (K)}=\mathbf{M}_{m,\varepsilon}^{(K)}\overline{\boldsymbol{\varepsilon}}_f^m,\ K\in[1,\ 56] \tag{13}$$

where the strains of yarns in the misalignment frame ($\overline{\boldsymbol{\varepsilon}}_f^m$) can be obtained by converting the strain components in the kinking frame ($\overline{\boldsymbol{\varepsilon}}_f^k$) through the following coordinate transformations:

$$\begin{cases}\overline{\varepsilon}_{f11}^m=\left(\overline{\varepsilon}_{f11}^k-\overline{\varepsilon}_{f22}^k\right)\cos^2\varphi+\overline{\varepsilon}_{f22}^k+\overline{\gamma}_{f12}^k\sin\theta\cos\theta\\ \overline{\varepsilon}_{f22}^m=\left(\overline{\varepsilon}_{f22}^k-\overline{\varepsilon}_{f11}^k\right)\cos^2\varphi+\overline{\varepsilon}_{f11}^k-\overline{\gamma}_{f12}^k\sin\theta\cos\theta\\ \overline{\varepsilon}_{f33}^m=\overline{\varepsilon}_{f33}^k\\ \overline{\gamma}_{f12}^m=2\left(\overline{\varepsilon}_{f22}^k-\overline{\varepsilon}_{f11}^k\right)\sin\theta\cos\theta+\overline{\gamma}_{f12}^k\cos 2\varphi\\ \overline{\gamma}_{f13}^m=\overline{\gamma}_{f13}^k\cos\varphi+\overline{\gamma}_{f23}^k\sin\varphi\\ \overline{\gamma}_{f23}^m=-\overline{\gamma}_{f13}^k\sin\varphi+\overline{\gamma}_{f23}^k\cos\varphi\end{cases} \tag{14}$$

where $\overline{\boldsymbol{\varepsilon}}_f^k$ in the kinking frame can be obtained by converting $\overline{\boldsymbol{\varepsilon}}_f$ in the axial frame:

$$\begin{cases}\overline{\varepsilon}_{f11}^k=\overline{\varepsilon}_{f11}\\ \overline{\varepsilon}_{f22}^k=\left(\overline{\varepsilon}_{f22}-\overline{\varepsilon}_{f33}\right)\cos^2\theta+\overline{\varepsilon}_{f33}+\overline{\gamma}_{f23}\sin\theta\cos\theta\\ \overline{\varepsilon}_{f33}^k=\left(\overline{\varepsilon}_{f33}-\overline{\varepsilon}_{f22}\right)\cos^2\theta+\overline{\varepsilon}_{f22}-\overline{\gamma}_{f23}\sin\theta\cos\theta\\ \overline{\gamma}_{f12}^k=\overline{\gamma}_{f12}\cos\theta+\overline{\gamma}_{f13}\sin\theta\\ \overline{\gamma}_{f13}^k=-\overline{\gamma}_{f12}\sin\theta+\overline{\gamma}_{f13}\cos\theta\\ \overline{\gamma}_{f23}^k=2\left(\overline{\varepsilon}_{f33}-\overline{\varepsilon}_{f22}\right)\sin\theta\cos\theta+\overline{\gamma}_{f23}\cos 2\theta\end{cases} \tag{15}$$

3.4. Yarns/matrix interface debonding

In this work, the yarn/matrix interface debonding is captured by cohesive zone model. The constitutive responses of the cohesive interface can be described by the following relations:

$$\sigma_n=(1-d)K_n\delta_n,\ \tau_s=(1-d)K_s\delta_s,\ \tau_t=(1-d)K_t\delta_t \tag{16}$$

where n, s and t indicate the normal and shear directions of the interface, respectively, and σ_n, τ_s, τ_t and δ_n, δ_s, δ_t indicate the related traction and displacement components. Considering the mixed-mode loadings within 3DWC, the quadratic stress criterion is adopted to detect the interface debonding initiations.

$$\left(\langle\sigma_n\rangle/\sigma_n^{\max}\right)^2+\left(\tau_s/\tau_s^{\max}\right)^2+\left(\tau_t/\tau_t^{\max}\right)^2=1 \tag{17}$$

where $\sigma_n^{\max}$, $\tau_s^{\max}$, $\tau_s^{\max}$ denote the critical strengths of the interface. The $\langle x\rangle$ operator means that the compressive normal traction has no influence on the debonding. Upon the initial interfacial debonding is detected, the gradual damage development is characterized by the linear softening scheme based on dissipated energies:

$$\left(G_n/G_n^C\right)^2+\left(G_s/G_s^C\right)^2+\left(G_t/G_t^C\right)^2=1 \tag{18}$$

where G_n, G_s and G_t represent the fracture energies associated with normal and shear damage modes, respectively, and G_n^C, G_s^C and G_t^C represent the related critical energies. Given that there are no accurate experimental data, the interface parameters in this paper are quoted from Ref. [31] because of the similar material system, where $\sigma_n^{\max}=50$ MPa, $\tau_s^{\max}=\tau_t^{\max}=70$ MPa, $G_n^C=2$, $G_s^C=G_t^C=30$ N/m, and $K_n=K_s=K_t=10^8$ MPa/mm.

4. Constitutive equations and numerical implementation

4.1. Constitutive equations with damage variable

The longitudinal and transverse load-bearing capacities of fiber bundles are associated with the damage variables $d_{f,kink}$ and $d_{f,m}$, respectively. Once $d_{f,m}$ and $d_{f,kink}$ are calculated through Eqs. (10) and (12), the damaged constitutive equations of yarns can be described by the following relations [41,42]:

$$\overline{\boldsymbol{\sigma}}_f=\mathbf{C}_f(d)\overline{\boldsymbol{\varepsilon}}_f \tag{19}$$

where $\mathbf{C}_f(d)$ can be further expressed as follows:

$$\begin{bmatrix}(1-d_{f,kink})C_{11} & (1-d_{f,kink})(1-d_{f,m})C_{12} & (1-d_{f,kink})(1-d_{f,m})C_{13} & 0 & 0 & 0\\ & (1-d_{f,m})C_{22} & (1-d_{f,m})C_{23} & 0 & 0 & 0\\ & & (1-d_{f,m})C_{33} & 0 & 0 & 0\\ & & & (1-d_s)C_{44} & 0 & 0\\ & SYM & & & (1-d_s)C_{55} & 0\\ & & & & & (1-d_s)C_{66}\end{bmatrix} \tag{20}$$

where the damage variable d_s related to shear performance can be calculated by:

$$d_s = 1 - \left(1 - d_{f,m}\right)\left(1 - d_{f,kink}\right) \tag{21}$$

After the matrix failure initiation, the performance of the matrix will continue to decrease with the increasing deformation. In this paper, the stress-strain relationships of matrix, including the damage variable, are defined as $\boldsymbol{\sigma}_m = (1 - d_m)\mathbf{C}_m\boldsymbol{\varepsilon}_m$.

4.2. Viscosity regularization and tangent constitutive tensors

It should be noted that damage evolution in implicit algorithms generally leads to great convergence difficulties. To avoid this problem, the Duvaut-Lions viscosity regularization [43] is conducted in this paper. The time derivatives of damage variables are defined as follows:

$$\dot{d}^v_{f,kink} = \frac{d_{f,kink} - d^v_{f,kink}}{\eta};\ \dot{d}^v_{f,m} = \frac{d_{f,m} - d^v_{f,m}}{\eta};\ \dot{d}^v_{m} = \frac{d_{m} - d^v_{m}}{\eta} \tag{22}$$

where η denotes the viscous parameter. The regularized damage variable of the $I-th$ analysis increment can be deduced by backward-Euler methods:

$$d^{v\ (I)}_{f,kink} = \frac{\Delta t d^{(I)}_{f,kink} + \eta d^{v\ (I-1)}_{f,kink}}{\eta + \Delta t};\ d^{v\ (I)}_{f,m} = \frac{\Delta t d^{(I)}_{f,m} + \eta d^{v\ (I-1)}_{f,m}}{\eta + \Delta t};\ d^{v\ (I)}_{m} = \frac{\Delta t d^{(I)}_{m} + \eta d^{v\ (I-1)}_{m}}{\eta + \Delta t} \tag{23}$$

where Δt is the time increment. It is known that accurate calculations of the tangent constitutive tensors are conducive to fast convergence rate for the numerical implicit algorithms. In this work, the tangent constitutive tensors in damage configurations can be deduced as follows:

$$\dot{\boldsymbol{\sigma}} = \mathbf{C}_T\dot{\boldsymbol{\varepsilon}}_f \Rightarrow \begin{cases} \mathbf{C}_{m,T} = \mathbf{C}_m(d) + \left[\dfrac{\partial \mathbf{C}_m(d)}{\partial d^v_m}\dfrac{\partial d^v_m}{\partial d_m}\dfrac{\partial d_m}{\partial \delta_{eq,m}}\dfrac{\partial \delta_{eq,m}}{\partial \boldsymbol{\varepsilon}}\right] : \boldsymbol{\varepsilon} \\ \mathbf{C}_{f,T} = \mathbf{C}_f(d) + \left[\dfrac{\partial \mathbf{C}_f(d)}{\partial d^v_{f,kink}}\dfrac{\partial d^v_{f,kink}}{\partial d_{f,kink}}\dfrac{\partial d_{f,kink}}{\partial \boldsymbol{\varepsilon}} + \dfrac{\partial \mathbf{C}_f(d)}{\partial d^v_{f,m}}\dfrac{\partial d^v_{f,m}}{\partial d_{f,m}}\dfrac{\partial d_{f,m}}{\partial \boldsymbol{\varepsilon}}\right] : \boldsymbol{\varepsilon} \end{cases} \tag{24}$$

The strain derivatives of the equivalent displacement for the matrix are presented in Appendix A. For the fiber yarns, the derivatives of $d_{f,kink}$ and $d_{f,m}$ with respect to the strain components of yarns are presented in Appendix B. The other terms in Eq. (24) can be simply calculated by the

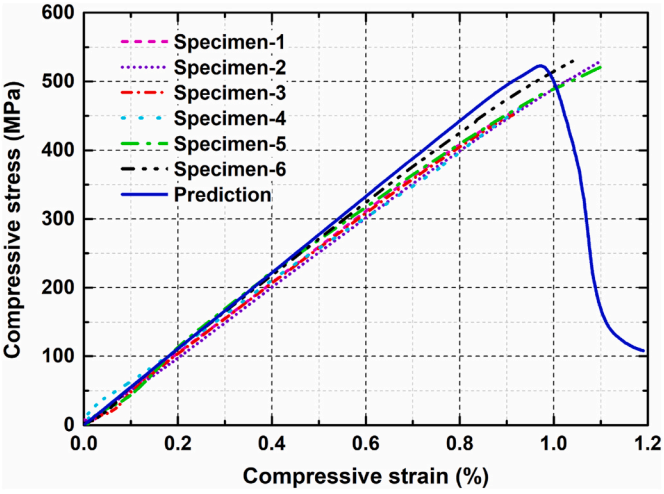

Fig. 7. Compressive stress-strain curves of the 3DWC in warp direction.

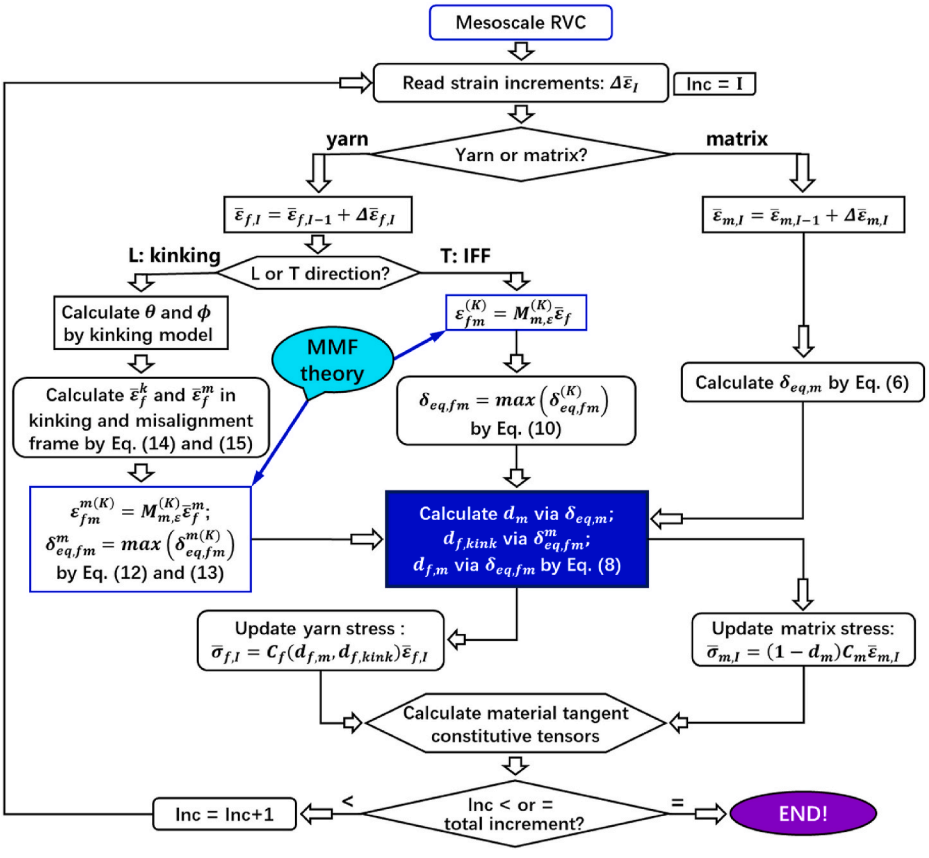

Fig. 6. The flow chart of the multiscale calculation procedure of 3D woven composites.

formula presented in previous sections.

4.3. Multiscale calculation procedure based on MMF theory

The flow chart of the multiscale calculation procedure of 3D woven composites under compressive loading based on MMF theory is briefly displayed in Fig. 6. The newly proposed damage model is numerically integrated into ABAQUS with a user-defined subroutine UMAT.

5. Results and discussion

5.1. Stress-strain relations and effective properties

The compressive stress-strain curve in warp direction of the 3DWC was predicted and displayed in Fig. 7, in comparison with the experimental curves taken from Ref. [9], where six specimens with two widths were tested. It can be seen that the slope and the peak point of the curve obtained by prediction are slightly higher than those of the experiment, and the overall agreement is good. Initially, the predicted curve rises in a linear relationship. As the loading increases, the slope gradually decreases due to the damage accumulations inside the composites. When exceeding the maximum compressive stress point, the reaction force will quickly drop to a small value. The experimental and predicted effective properties of 3DWC are listed in Table 2, including the strengths, modulus and failure strains. The experimental results exhibit a certain degree of dispersion. The standard deviations of the strength, modulus and failure strain obtained by the experiments are 36.43 MPa, 2.72 GPa, and 0.084%, respectively, which are 7.35%, 5.13%, and 8.35% of the corresponding experimental averages, respectively. The average strength, modulus and failure strain are 495.47 MPa, 53.03 GPa and 1.01% respectively, while the corresponding values obtained by the prediction are 522.95 MPa, 55.47 GPa, and 0.97% respectively. The errors of the results are all within 6%, which are less than the experimental standard deviations, indicating the reliability and accuracy of the new micromechanics-based multiscale damage model.

5.2. Damage accumulation process

The initial damage locations and damaged element percentages corresponding to different failure mechanisms of 3DWC under compressive loading in warp direction are illustrated in Fig. 8. Damage element percentage is defined to measure the severity of failure, which can be obtained by dividing the number of damaged elements by the number of component elements. As can be seen, the fiber kinking $d_{f,kink}$ in warp tows, inter-fiber fracture $d_{f,m}$ in fiber tows, matrix failure d_m and tows/matrix interfacial debonding *SDEG*, continue to accumulate as the compressive load increases. The detailed damage accumulation process of the meso RVC is intuitively displayed in Fig. 9, and the compressive strains at I, II and III locations are 0.80%, 0.97% and 1.10%, respectively. When the compressive strain is 0.44%, the interface debonding first occurs in the area where the binder tow and the matrix are squeezed. Then, the inter-fiber fracture is detected due to the weaker transverse load-bearing capacity of fiber tows. The matrix is not prone to failure because of the hydrostatic pressure under compressive loads, thus only a small amount of matrix failure appear in the stress concentration area at 0.67% strain. Finally, the fiber kinking in longitudinal tows initiates at 0.84% strain. After the final rupture of the meso RVC, the various failure mechanisms quickly accumulate in a short strain range. In the end, about 80% of the fiber elements suffer inter-fiber fracture, about 70% of warp elements suffer kinking failure and most of the interfaces are debonding, while there are few failure matrix elements.

Table 2
The experimental and predicted effective properties of the 3DWC.

warp compression [9]	strengths (MPa)	modulus (GPa)	failure strains (%)
Specimen-1	465.71	52.38	0.94
Specimen-2	531.64	48.73	1.10
Specimen-3	451.49	51.84	0.91
Specimen-4	471.34	53.49	0.95
Specimen-5	522.80	56.37	1.10
Specimen-6	529.81	55.34	1.04
Average	495.47	53.03	1.01
Prediction	522.95	55.47	0.97
errors/%	5.55	4.60	3.96

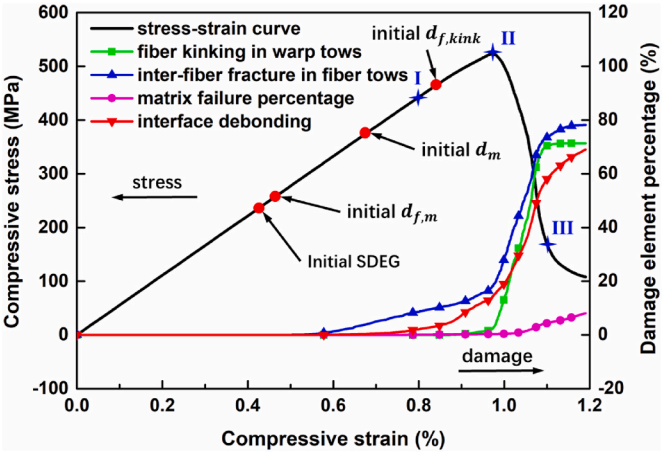

Fig. 8. The initial damage locations and damaged element percentages of the 3DWC under compressive loading in warp direction.

5.3. Influence of initial misalignment angle of fiber yarns

In this paper, a novel method incorporating the MMF theory [17] and 3D kinking model [16] is developed to identify the kinking failure of fiber yarns at the micro-scale. The fiber kinking failure is mainly caused by the longitudinal compressive stress σ_{11} and shear stress τ_{12} [15]. Based on the newly developed method, the kinking failure envelopes displayed in Fig. 10 of fiber tows with varied initial misalignment φ_0 under combined σ_{11} and τ_{12} stresses can be obtained. The compressive strengths of kinking failure are greatly sensitive to the fiber initial misalignments. As the shear stress increases, the compressive strength approximately presents a linear decreasing trend. When the shear stress increases to approach the shear strength, the envelope curves exhibit a slight nonlinearity.

In reality, the fiber initial misalignments are randomly distributed throughout the experimental samples. In this paper, the normal probabilistic functions are employed to characterize such stochastic distributions. A user-defined subroutine SDVINI is written to assign the stochastic φ_0 to each fiber element. As shown in Fig. 11, the initial misalignment angle in the mesoscopic RVC model varies from element to element and obeys the normal distribution. The influences of the initial misalignments on the compressive properties of 3DWC were investigated by conducting a parametrical study. The stress-strain curves of the meso RVC with six varied φ_0 ranges are displayed in Fig. 11. The fiber initial misalignments have obvious influences on the compression failure strength and strain. Due to the different random seeds generated each time, the predicted curves with the same φ_0 range exhibit small difference between each other. As the normal distribution range increases, the predicted strengths and strains gradually decrease. The meso RVC without fiber initial misalignment provides slightly overestimated predictions compared to the experimental results, but the differences are accepted as mentioned in Section 5.1. It should be noted that the fiber tows inside 3DWC undulate, thus even a simple uniaxial compression will lead to a certain fraction of shear stress. The greater the undulation amplitude, the greater the shear stress. Therefore, even if the fiber initial misalignment is not introduced, acceptable prediction

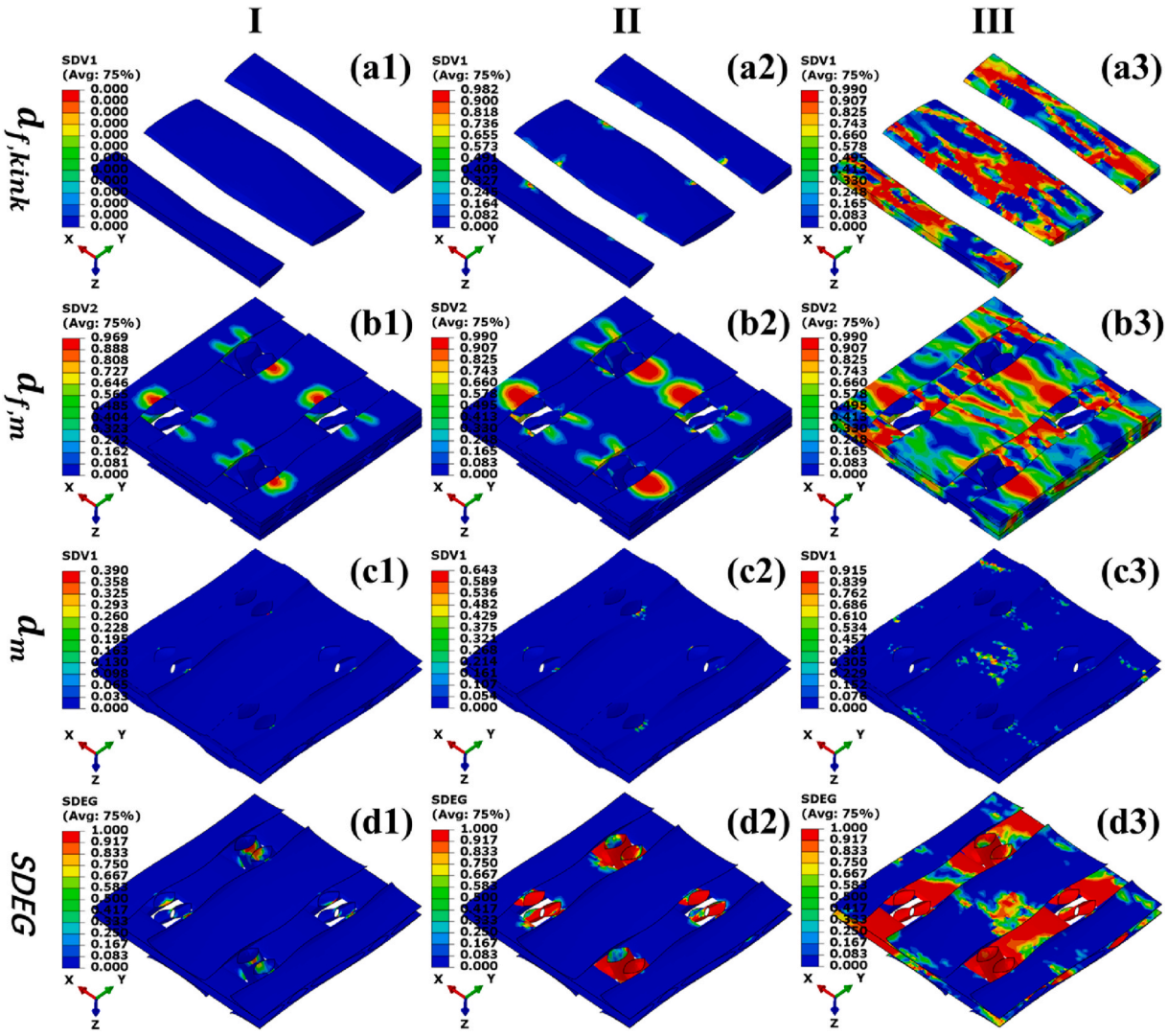

Fig. 9. The damage accumulations of the meso RVC: damage related to $d_{f,kink}$ in warp tow (a1)-(a3), $d_{f,m}$ in fiber tows (b1)-(b3), matrix failure d_m (c1)-(c3), interface debonding between tows and matrix (d1)-(d3).

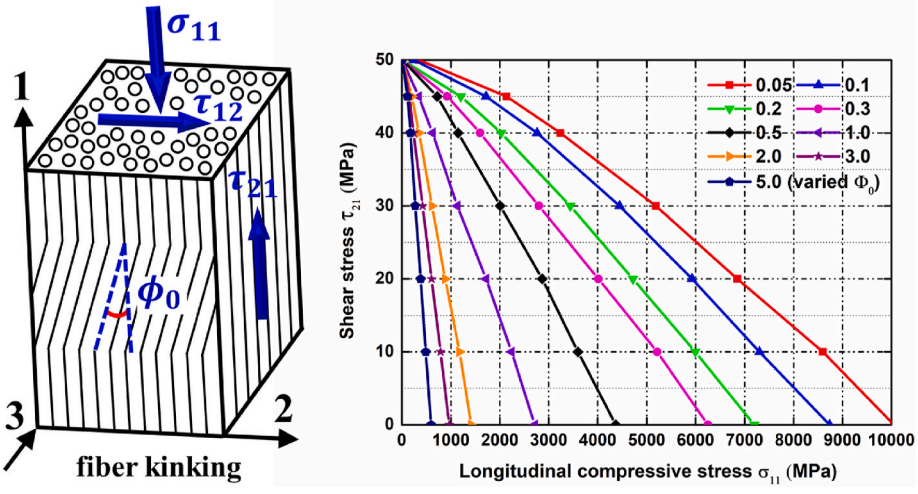

Fig. 10. Kinking failure envelopes of tows with varied φ_0 under σ_{11} versus τ_{12} stresses.

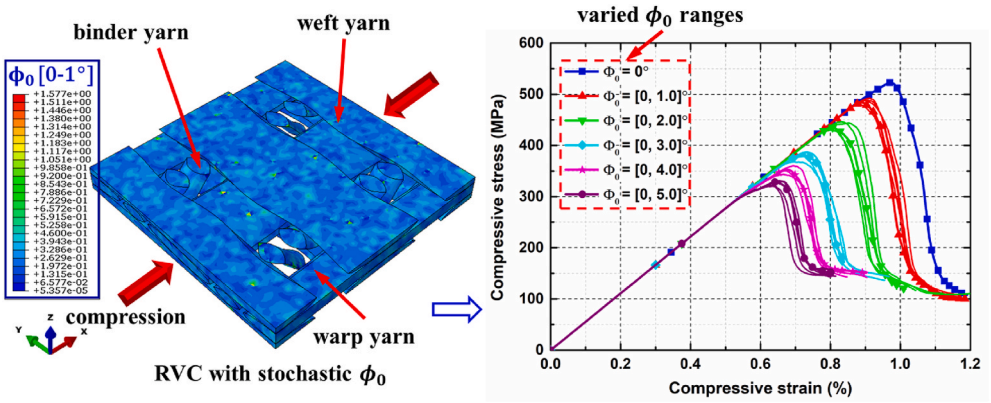

Fig. 11. The influences of stochastic initial misalignment on the compressive properties of 3DWC: (a) RVC model with stochastic φ_0; (b) Stress-strain curves with varied φ_0 ranges.

results can be obtained as long as the woven architecture is realistically constructed. Nevertheless, the introduction of appropriate fiber initial misalignment distributions can obtain more precise predictions that are more consistent with the experiments. Moreover, the experimental results present obvious dispersion, which may be attributed to the randomly distributed initial imperfections in the actual specimens. Thus it is more reasonable to adopt the stochastic φ_0 distribution for numerical simulations to characterize the scattered experimental results.

5.4. Discussion on matrix plasticity and initial residual stress

It should be noted that the matrix material studied in the present work is very brittle, and that the model presently does not include the effect of matrix plasticity. Therefore it could be expected that the model's prediction accuracy might be lower for a composite containing a more ductile resin. Adding the capability to account for matrix plasticity in future work might increase the applicability of the model.

It is known that initial residual stresses can cause an apparent reduction of the strength of cured fiber tows and textile composites. Heinrich et al. [44] and D'Mello and Waas [45,46] have proposed a virtual manufacturing model to calculate these stresses. However, this method requires certain properties that need to be measured during the actual curing process. In the present study, the material was supplied in a cured state, and the material properties required for the virtual manufacturing method were not available. Therefore the present model does not model the effect of residual stresses. This is something that could be added in future work to increase the accuracy of the model.

6. Conclusion

A novel micromechanics-based multiscale progressive damage model is presented in this work to investigate the compressive failure behaviours of 3D woven composites with minimal material parameters. The highly realistic constructions of microscopic and mesoscopic representative volume cells (RVC) were first accomplished, then the MMF theory was employed to bridge the meso-scale and micro-scale calculations by introducing a set of SSAF. Some important conclusions can be summarized as follows:

(1) The micromechanics-based multiscale model was adopted to predict the rupture strength and failure behaviors of 3DWC submitted to compressive loadings. The numerical predictions were compared with the experiments, and a good agreement (within 6% in terms of strength, failure strain, and stiffness) was obtained, which verifies the feasibility and accuracy of the model.

(2) The newly proposed multiscale damage model identifies the micro matrix failure associated with the kinking of yarns, inter-fiber fracture and pure matrix failure by developing a new method incorporating the MMF theory and 3D kinking model. As a result, only matrix parameters are employed to predict the damage initiations and evolutions and good agreement with experimental results was achieved. This verifies the feasibility of modelling the compressive failure mechanisms of 3DWC without using other material parameters such as the fracture toughness and failure strengths of the yarns, which are generally difficult to accurately obtain through experiments.

(3) The influences of stochastic initial fiber misalignments on the compressive properties of 3DWC were estimated by conducting a parametrical study. It was observed that the fiber initial misalignments had great influences on the compression failure strength and strain. Additionally, appropriate introduction of fiber initial misalignment distributions can obtain more precise predictions and characterize the scatter of experimental results.

CRediT author statement

Tao Zheng: Formal analysis, Conceptualization, Methodology, Investigation, Software, Validation, Writing-Original Draft.

Licheng Guo: Supervision, Conceptualization, Writing - Review & Editing.

Rinze Benedictus: Supervision, Writing - Review & Editing.

John-Alan Pascoe: Supervision, Methodology, Writing - Review & Editing.

Declaration of competing interest

The authors declare that they have no known competing financial interests or personal relationships that could have appeared to influence the work reported in this paper.

Acknowledgements

This work was sponsored by National Natural Science Foundation of China (11972134), Natural Science Foundation of Heilongjiang Province (ZD2019A001) and China Scholarship Council (CSC NO.202006120106, Joint-training PhD project).

Appendix A. The strain derivatives of the equivalent displacement for the matrix

For the pure matrix, the strain derivatives of the equivalent displacement in Eq. (24) can be expanded as:

$$\frac{\partial \delta_{eq,m}}{\partial \varepsilon_{m,j}} = \frac{\partial \delta_{eq,m}}{\partial J_1}\frac{\partial J_1}{\partial \varepsilon_{m,j}} + \frac{\partial \delta_{eq,m}}{\partial \varepsilon_{VM}}\frac{\partial \varepsilon_{VM}}{\partial \varepsilon_{m,j}} \tag{A.1}$$

where the specific items in Eq. (A.1) can be further expressed as follows:

$$\begin{cases} \dfrac{\partial \delta_{eq,m}}{\partial J_1} = l_{c,m}\left\{(\beta-1) + J_1(\beta-1)^2\left[\left(\dfrac{2-4\nu_m}{1+\nu_m}\right)^2\beta\varepsilon_{VM}^2 + (\beta-1)^2 J_1^2\right]^{-1/2}\right\} \Big/ [2\beta(1-2\nu_m)] \\ \dfrac{\partial \delta_{eq,m}}{\partial \varepsilon_{VM}} = l_{c,m}\beta\varepsilon_{VM}\left(\dfrac{2-4\nu_m}{1+\nu_m}\right)^2\left[\left(\dfrac{2-4\nu_m}{1+\nu_m}\right)^2\beta\varepsilon_{VM}^2 + (\beta-1)^2 J_1^2\right]^{-1/2} \Big/ [2\beta(1-2\nu_m)],\ \beta = m_c \Big/ m_t \\ \dfrac{\partial J_1}{\partial \varepsilon_{m11}} = \dfrac{\partial J_1}{\partial \varepsilon_{m22}} = \dfrac{\partial J_1}{\partial \varepsilon_{m33}} = 1;\ \dfrac{\partial J_1}{\partial \gamma_{m12}} = \dfrac{\partial J_1}{\partial \gamma_{m13}} = \dfrac{\partial J_1}{\partial \gamma_{m23}} = 0 \\ \dfrac{\partial \varepsilon_{VM}}{\partial \varepsilon_{m11}} = \dfrac{1}{2\varepsilon_{VM}}(2\varepsilon_{m11} - \varepsilon_{m22} - \varepsilon_{m33});\ \dfrac{\partial \varepsilon_{VM}}{\partial \varepsilon_{m22}} = \dfrac{1}{2\varepsilon_{VM}}(2\varepsilon_{m22} - \varepsilon_{m11} - \varepsilon_{m33}) \\ \dfrac{\partial \varepsilon_{VM}}{\partial \varepsilon_{m33}} = \dfrac{1}{2\varepsilon_{VM}}(2\varepsilon_{m33} - \varepsilon_{m11} - \varepsilon_{m22});\ \dfrac{\partial \varepsilon_{VM}}{\partial \gamma_{m12}} = \dfrac{3}{4\varepsilon_{VM}}\gamma_{m12} \\ \dfrac{\partial \varepsilon_{VM}}{\partial \gamma_{m13}} = \dfrac{3}{4\varepsilon_{VM}}\gamma_{m13};\ \dfrac{\partial \varepsilon_{VM}}{\partial \gamma_{m23}} = \dfrac{3}{4\varepsilon_{VM}}\gamma_{m23} \end{cases} \tag{A.2}$$

Appendix B. The strain derivatives of $d_{f,kink}$ and $d_{f,m}$ for the fiber yarns

For the fiber yarns, the derivatives of $d_{f,kink}$ and $d_{f,m}$ with respect to the strain components of yarns can be expanded as:

$$\begin{cases} \dfrac{\partial d_{f,m}}{\partial \varepsilon_{f,j}} = \dfrac{\partial d_{f,m}}{\partial \delta_{eq,fm}}\left[\dfrac{\partial \delta_{eq,fm}}{\partial J_1}\sum_L \dfrac{\partial J_1}{\partial \varepsilon_{fm,L}}\dfrac{\partial \varepsilon_{fm,L}}{\partial \varepsilon_{f,j}} + \dfrac{\partial \delta_{eq,fm}}{\partial \varepsilon_{VM}}\sum_L \dfrac{\partial \varepsilon_{VM}}{\partial \varepsilon_{fm,L}}\dfrac{\partial \varepsilon_{fm,L}}{\partial \varepsilon_{f,j}}\right] \\ \dfrac{\partial d_{f,kink}}{\partial \varepsilon_{f,j}} = \dfrac{\partial d_{f,kink}}{\partial \delta^m_{eq,fm}}\left[\begin{array}{l} \dfrac{\partial \delta^m_{eq,fm}}{\partial J_1}\sum_L \dfrac{\partial J_1}{\partial \varepsilon^m_{fm,L}}\sum_M \dfrac{\partial \varepsilon^m_{fm,L}}{\partial \varepsilon^m_{f,M}}\sum_N \dfrac{\partial \varepsilon^m_{f,M}}{\partial \varepsilon^k_{f,N}}\dfrac{\partial \varepsilon^k_{f,N}}{\partial \varepsilon_{f,j}} + \\ \dfrac{\partial \delta^m_{eq,fm}}{\partial \varepsilon_{VM}}\sum_L \dfrac{\partial \varepsilon_{VM}}{\partial \varepsilon^m_{fm,L}}\sum_M \dfrac{\partial \varepsilon^m_{fm,L}}{\partial \varepsilon^m_{f,M}}\sum_N \dfrac{\partial \varepsilon^m_{f,M}}{\partial \varepsilon^k_{f,N}}\dfrac{\partial \varepsilon^k_{f,N}}{\partial \varepsilon_{f,j}} \end{array}\right] \end{cases} \tag{B.1}$$

It is noted that $\varepsilon_L;\varepsilon_M;\varepsilon_N;\varepsilon_j = (\varepsilon_{11},\varepsilon_{22},\varepsilon_{33},\gamma_{12},\gamma_{13},\gamma_{23})$ in Eq. (B.1). The superscripts m and k of the strain components indicate the misalignment frame and kinking frame, respectively, and the subscripts fm and f indicate the micro strains within yarns and meso strains of yarns, respectively. According to the strain amplification factor, $\partial \varepsilon_{fm,L}/\partial \varepsilon_{f,M} = M_{m,\varepsilon}(L,M)$. The other terms in Eq. (B.1) can be simply calculated by the formula presented in previous sections.

References

[1] A.P. Mouritz, M.K. Bannister, P.J. Falzon, K.H. Leong, Review of applications for advanced three-dimensional fibre textile composites, Compos. Part A-Appl. S. 30 (1999) 1445–1461.

[2] F. Boussu, I. Cristian, S. Nauman, General definition of 3D warp interlock fabric architecture, Compos. B Eng. 81 (2015) 171–188.

[3] B. Budiansky, N.A. Fleck, Compressive failure of fibre composites, J. Mech. Phys. Solid. 41 (1) (1993) 183–211.

[4] S.C. Quek, A.M. Waas, K.W. Shahwan, V. Agaram, Compressive response and failure of braided textile composites: Part 1 - experiments, Int J. Nonlinear Mech. 39 (4) (2003) 635–648.

[5] M. Pankow, A.M. Waas, C.F. Yen, S. Ghiorse, Split-hopkinson pressure bar testing of 3D woven composites, Compos. Sci. Technol. 71 (9) (2011) 1196–1208.

[6] H. Huang, A.M. Waas, Compressive response of Z-pinned woven glass fiber textile composite laminates: Experiments, Compos. Sci. Technol. 69 (14) (2009) 2331–2337.

[7] D. Zhang, A.M. Waas, C.F. Yen, Progressive damage and failure response of hybrid 3D textile composites subjected to flexural loading, part I: experimental studies, Int. J. Solid Struct. 75–76 (2015) 309–320.

[8] D.K. Patel, A.M. Waas, C.F. Yen, Compressive response of hybrid 3D woven textile composites (H3DWTCs): an experimentally validated computational model, J. Mech. Phys. Solid. 122 (2019) 381–405.

[9] T. Zheng, L. Guo, R. Sun, Z. Li, H. Yu, Investigation on the compressive damage mechanisms of 3D woven composites considering stochastic fiber initial misalignment, Compos. Part A-Appl. S. 143 (2021) 106295.

[10] Z. Hashin, Failure criteria for unidirectional fiber composites, J. Appl. Mech. 47 (1980) 329–334.

[11] F.K. Chang, K.Y. Chang, A progressive damage model for laminated composites containing stress concentrations, J. Compos. Mater. 21 (9) (1987) 834–855.

[12] F.K. Chang, L.B. Lessard, Damage tolerance of laminated composites containing an open hole and subjected to compressive loadings: Part I-analysis, J. Compos. Mater. 25 (1) (1991) 2–43.

[13] A. Puck, H. Schürmann, Faliure analysis of FRP laminates by means of physically based phenomenological models, Compos. Sci. Technol. 58 (7) (1998) 1045–1067.

[14] A. Puck, J. Kopp, M. Knops, Guidelines for the determination of the parameters in Puck's action plane strength criterion, Compos. Sci. Technol. 62 (3) (2002) 371–378.

[15] C.G. Dávila, P.P. Camanho, C.A. Rose, Failure criteria for FRP laminates, J. Compos. Mater. 39 (4) (2005) 323–345.

[16] S.T. Pinho, L. Iannucci, P. Robinson, Physically based failure models and criteria for laminated fibre-reinforced composites with emphasis on fibre kinking. Part II: FE implementation, Compos. Part A-Appl. S. 37 (5) (2006) 766–777.

[17] S.K. Ha, K.K. Jin, Y. Huang, Micro-mechanics of failure (MMF) for continuous fiber reinforced composites, J. Compos. Mater. 42 (18) (2008) 1873–1895.

[18] K.K. Jin, Y. Huang, Y.H. Lee, S.K. Ha, Distribution of micro stresses and interfacial tractions in unidirectional composites, J. Compos. Mater. 42 (18) (2008) 1825–1849.

[19] Y. Huang, L. Xu, S.K. Ha, Prediction of three-dimensional composite laminate response using micromechanics of failure, J. Compos. Mater. 46 (19–20) (2012) 2431–2442.

[20] Y. Huang, C. Jin, S.K. Ha, Strength prediction of triaxially loaded composites using a progressive damage model based on micromechanics of failure, J. Compos. Mater. 47 (6–7) (2012) 777–792.
[21] D. Zhang, A.M. Waas, A micromechanics based multiscale model for nonlinear composites, Acta Mech. 225 (4–5) (2014) 1391–1417.
[22] D.K. Patel, A.D. Hasanyan, A.M. Waas, N-Layer concentric cylinder model (NCYL): an extended micromechanics-based multiscale model for nonlinear composites, Acta Mech. 228 (2017) 275–306.
[23] M. Zako, Y. Uetsuji, T. Kurashiki, Finite element analysis of damaged woven fabric composite materials, Compos. Sci. Technol. 63 (2003) 507–516.
[24] M.M. Shokrieh, L.B. Lessard, Progressive fatigue damage modeling of composite materials. part 1: Modeling, J. Compos. Mater. 34 (13) (2000) 1056–1080.
[25] G. Fang, J. Liang, B. Wang, Progressive damage and nonlinear analysis of 3D four-directional braided composites under unidirectional tension, Compos. Struct. 89 (1) (2009) 126–133.
[26] I. Lapczyk, J.A. Hurtado, Progressive damage modeling in fiber-reinforced materials, Compos. Part A-Appl. S. 38 (11) (2007) 2333–2341.
[27] Z.P. Bažant, B.H. Oh, Crack band theory for fracture of concrete, Mater. Struct. 16 (1983) 155–177.
[28] P. Maimí, P.P. Camanho, J.A. Mayugo, C.G. Dávila, A continuum damage model for composite laminates: Part II – computational implementation and validation, Mech. Mater. 39 (10) (2007) 909–919.
[29] D. Zhang, A.M. Waas, C.F. Yen, Progressive damage and failure response of hybrid 3D textile composites subjected to flexural loading, part II: mechanics based multiscale computational modeling of progressive damage and failure, Int. J. Solid Struct. 75–76 (2015) 321–335.
[30] S. Zhong, L. Guo, G. Liu, H. Lu, T. Zeng, A continuum damage model for three-dimensional woven composites and finite element implementation, Compos. Struct. 128 (2015) 1–9.
[31] C. He, J. Ge, D. Qi, J. Gao, Y. Chen, J. Liang, D. Fang, A multiscale elasto-plastic damage model for the nonlinear behavior of 3D braided composites, Compos. Sci. Technol. 171 (2019) 21–33.
[32] B.G. Falzon, P. Apruzzese, Numerical analysis of intralaminar failure mechanisms in composite structures. Part II: Applications, Compos. Struct. 93 (2) (2011) 1047–1053.
[33] C. Zhang, W.K. Binienda, R.K. Goldberg, L.W. Kohlman, Meso-scale failure modeling of single layer triaxial braided composite using finite element method, Compos. Part A-Appl. S. 58 (2014) 36–46.
[34] Z. Zhao, P. Liu, C. Chen, C. Zhang, Y. Li, Modeling the transverse tensile and compressive failure behavior of triaxially braided composites, Compos. Sci. Technol. 172 (2019) 96–107.
[35] H. Kang, Z. Shan, Y. Zang, F. Liu, Progressive damage analysis and strength properties of fiber-bar composites reinforced by three-dimensional weaving under uniaxial tension, Compos. Struct. 141 (2016) 264–281.
[36] T. Zheng, L. Guo, J. Huang, G. Liu, A novel mesoscopic progressive damage model for 3D angle-interlock woven composites, Compos. Sci. Technol. 185 (2020) 107894.
[37] Y. Huang, K.K. Jin, S.K. Ha, Effects of fiber arrangement on mechanical behavior of unidirectional composites, J. Compos. Mater. 42 (18) (2008) 1851–1871.
[38] R. Raghava, R.M. Caddell, G.S.Y. Yeh, The macro-scopic yield behavior of polymers, J. Mater. Sci. 8 (1973) 225–232.
[39] F. Stassi-D'Alia, Flow and fracture of materials according to a new limiting condition of yielding, Meccanica 2 (3) (1967) 178–195.
[40] A.S. Argon, Fracture of composites, in: H. Herman (Ed.), Treatise on Materials Science and Technology, Academic Press, New York, 1972, pp. 79–114.
[41] A.L. Highsmith, K.L. Reifsnider, Stiffness-reduction mechanisms in composite laminates, in: K.L. Reifsnider (Ed.), Damage in Composite Materials, ASTM International, West Conshohocken, 1982, pp. 103–117.
[42] L. Wang, C. Zheng, S. Wei, Z. Wei, Micromechanics-based progressive failure analysis of carbon fiber/epoxy composite vessel under combined internal pressure and thermomechanical loading, Compos. B Eng. 89 (2016) 77–84.
[43] G. Duvaut, J.L. Lions, Inequalities in Mechanics and Physics, Springer, Berlin, 1976.
[44] C. Heinrich, M. Aldridge, A.S. Wineman, J. Kieffer, A.M. Waas, K.W. Shawan, The role of curing stresses in subsequent response, damage and failure of textile polymer composites, J. Mech. Phys. Solid. 61 (5) (2013) 1241–1264.
[45] R.J. D'Mello, M. Maiaru, A.M. Waas, Virtual manufacturing of composite aerostructures, Aeronaut. J. 120 (1223) (2016) 61–81.
[46] R.J. D'Mello, A.M. Waas, Virtual curing of textile polymer matrix composites, Compos. Struct. 178 (2017) 455–466.